Ambient temperature aqueous synthesis of ultrasmall copper doped ceria nanocrystals for the water gas shift and carbon monoxide oxidation reactions†

Christopher D. Curran,[a] Li Lu, [b] Christopher J. Kiely[ab] and Steven McIntosh *[a]

Ceria substitutionally doped with copper is a promising heterogeneous catalyst for a range of oxidation reactions. Herein we describe the aqueous phase, scalable, and direct precipitation of $Cu_xCe_{1-x}O_{2-d}$ ($x = 0–0.35$) solid solution oxide nanocrystals at room temperature without the need for calcination at elevated temperatures. This direct precipitation of the crystalline oxide is enabled through ligand exchange prior to pH adjustment to prevent the precipitation of the hydroxide phase. By producing particles at room temperature, dopant exsolution and particle growth by sintering can be minimized and/or controlled. Using our methodology, copper dopant concentrations of up to 35 mol% could be produced in 1.7 nm diameter ceria nanocrystals. The resulting materials showed high catalytic activity towards both the water gas shift reaction (WGS) and CO oxidation, with improved performance following the trend of increasing copper content. In comparison to pure ceria nanocrystals, the WGS activation energy decreased from 89.0 to 49.2 kJ mol^{-1} and the CO oxidation light-off temperature decreased from 262 to 159 C at a space velocity of 25 000 h^{-1} upon doping with 35 mol% copper.

Introduction

Copper–cerium mixed oxide materials are of considerable interest in a variety of catalytic applications such as the water gas shi (WGS) and CO oxidation reactions.[1–7] Both of these reactions have important signi cance in the industrial and automotive sectors. WGS catalysts are used for hydrogen and ammonia production at the industrial scale, and are an important component in fuel processors for proton-exchange membrane fuel cells, preventing CO poisoning at the anode.[6,8,9] In automobiles and stationary combustion sources, CO oxidation catalysts are widely used to mitigate the environmental impact of CO emissions and are an essential part of three-way catalyst systems.[10–12] Copper–cerium mixed oxide catalysts show high activity for these reactions due to the favorable redox properties of ceria and the active site created by incorporating copper. Additionally, the relatively low cost and earth-abundance of the constituent elements makes synthesis of these materials economical and scalable. While high copper dopant concentration and small particle size are desirable for enhancing this catalytic activity, the elevated temperatures associated with most synthesis procedures leads to exsolution of the dopant as well as particle growth. These two factors limit the accessible copper doping concentration and as-synthesized particle size. In this work, we describe a new synthesis protocol for the direct aqueous phase synthesis of ultrasmall highly doped copper–ceria nanocrystals and demonstrate their high activity towards the water gas shi and CO oxidation reactions.

There is general agreement in the literature that both copper and ceria play important roles in catalysis. While researchers agree on the importance of the redox capability of ceria through the Mars–van-Krevelen mechanism,[13,14] which has been demonstrated in ceria doped with other transition metals,[15–17] the precise nature of the Cu active site for both CO oxidation and the water gas shi reaction over $Cu_xCe_{1-x}O_{2-d}$ catalysts is still a matter for ongoing debate.[1,2] For example, Wang et al. and Gamarra et al. propose that CuO_x clusters on the catalyst surface are critical for the selective oxidation of CO.[1,3,4] However, Liu and Flytzani-Stephanopoulos have presented contradictory evidence showing that Cu(I) ions incorporated within the ceria lattice are the active sites.[5,18] The oxidation state of the Cu

[a]Department of Chemical and Biomolecular Engineering, Lehigh University, 111 Research Drive, Bethlehem, PA 18015, USA. E-mail: mcintosh@lehigh.edu

[b]Department of Materials Science and Engineering, Lehigh University, 5 East Packer Avenue, Bethlehem, PA 18015, USA

† Electronic supplementary information (ESI) available: TGA analysis demonstrating vaporization of moisture and capping ligands; elemental analysis of residual precursor a er precipitation; photograph of the Cu/lactic acid/ammonia system at various pH values; XRD spectra and GSAS tting of the $Cu_{0.35}Ce_{0.65}O_{2-d}$ sample; interplanar spacing and angles as determined through HAADF-STEM FFT analysis; Raman spectra of $Cu_{1-x}Ce_xO_{2-d}$ samples; XPS spectra of as-synthesized copper doped ceria samples; lightoff curves for WGS reaction with copper–ceria catalysts; HAADF-STEM micrographs of supported $Cu_{0.35}Ce_{0.65}O_{2-d}$ particles; XRD of pure ceria nanoparticles produced with varying lactic acid concentration.

species will be a strong function of reaction conditions, depending on whether one is dealing with total CO oxidation in excess O_2 or selective CO oxidation in the presence of H_2. Elias et al. proposed that Cu can exist at a higher oxidation state under reaction conditions of high oxygen partial pressure and that the active sites are oxygen vacancies formed adjacent to Cu-substituted surface sites in the mixed oxide nanoparticles.[2]

Despite this debate, there is some consensus that surface and near-surface enrichment of copper occurs under reaction conditions as the copper content in $Cu_xCe_{1\ x}O_{2\ d}$ increases, most likely leading to the formation of some CuO_x phase. However, there seems to be some clear advantages of fabri-cating these samples initially as intimately mixed solid solu-tions rather than depositing Cu directly onto pre-formed CeO_2. For example, Gamarra et al. speci cally compared the CO selective oxidation activity of co-precipitated $Cu_xCe_{1\ x}O_{2\ d}$ catalysts to the activity of supported CuO_x on CeO_2.[4] They noted that the high copper dispersion and initial presence of Cu in the co-precipitated catalyst leads to higher activity in the CO oxidation reaction.

Doped ceria materials are most commonly synthesized through ame aerosol pyrolysis,[19] co-precipitation,[20] or hydro-thermal routes.[21] These synthesis methods require high temperatures to generate crystalline products; however, expo-sure to high temperatures during synthesis can lessen the catalytic potential of the materials in two ways. Firstly, phase separation and migration of copper out of the ceria lattice can occur at high temperature, which limits the degree of interac-tion between copper and ceria. Secondly, high temperature processing can lead to increased crystallite size in the nal doped ceria product which in turn decreases the oxygen mobility, an important factor for reactions involving the Mars– van-Krevelen mechanism as oxygen vacancy concentration tends to be highest in small ceria crystallites.[22,23]

As described in a classic paper by Livage et al.[24] direct precipitation of the metal oxide from an aqueous phase metal nitrate or metal chloride precursor would require an elevated pH. As the pH of the reaction mixture increases, the interaction of the metal with the aqueous solution transitions from "aquo" (M–OH_2) to "hydroxo" (M–OH) and nally to "oxo" (M–O). Addition of typical precipitants, such as sodium hydroxide or ammonium hydroxide, raises the pH into the "hydroxo" region, leading to dissociation of any weakly bound NO_3 or Cl ligands and precipitation of metal hydroxide particles. These then require a high temperature calcination step to form metal oxide particles. Ligands utilized in sol–gel processing, such as ethylenediaminetetraacetic acid (EDTA), can prevent hydroxide precipitation, however their strong binding also prevents oxide precipitation,[25] once again requiring a calcination step to remove the ligand and transform to the metal oxide.

In this study, we demonstrate a facile method for direct formation of copper cerium oxide nanocrystals at room temperature in aqueous solution. This approach exchanges the nitrate ligands present in a mixed cerium nitrate and copper nitrate precursor solution for the intermediate strength lactate ligand, to shi the precipitation pH from the "hydroxo" to the "oxo" regime. Inducing precipitation via addition of ammonium hydroxide then leads to direct formation of <4 nm diameter $Cu_xCe_{1\ x}O_{2\ d}$ nanocrystals in the aqueous phase at room temperature. The Cu content can be tuned through the Cu nitrate/Ce nitrate ratios in the initial precursor solution to achieve as-synthesized Cu contents up to x ¼ 35 in $Cu_xCe_{1\ x}$-$O_{2\ d}$. We demonstrate that these two factors make our nano-particles excellent candidate materials for CO oxidation and water gas shi reaction catalysts.

Experimental methods

Particle synthesis

We synthesized ceria based nanoparticles using a modi ed base precipitation method as shown schematically in Fig. 1. 100 mL of aqueous solution was prepared with 100 mM $Ce(NO_3)_3$, 0–200 mM $Cu(NO_3)_2$ and a DL-lactic acid concentration equal to the total solution nitrate concentration ([$CH_3CHCOOH$] ¼ [NO_3]). While stirring (500 rpm), nanoparticle growth was initiated by raising the pH to between 8.5 and 9 through the dropwise addition of 6% ammonium hydroxide solution. This pH was maintained for 2 h and the solution was allowed to stir overnight. A er particle synthesis, excess lactic acid, nitric acid and ammonia were removed by dialysis using Thermo Snake-skin 3500 kDa tubing against deionized water, which caused aggregation of the mixed oxide particles. The solid product was washed three times by centrifugation (10 000 RCF) and subse-quent re-suspension in deionized water. The nanoparticles were nally re-dispersed and stored in dilute citric acid buffer (20 mM, pH 5.5) until required for use.

Materials characterization

Samples for scanning electron microscopy (SEM) and energy dispersive X-ray (XEDS) analysis were prepared by drying the nanoparticle sols at room temperature, under vacuum over-night and attaching the dried lm to an Al sample stub using

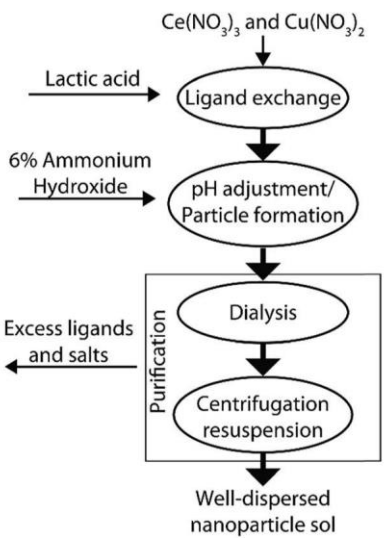

Fig. 1 Synthesis flow diagram for the synthesis of our $Cu_xCe_{1\ x}O_{2\ d}$ nanoparticle sols.

adhesive carbon tape. The samples were examined in a Hitachi 4300SE SEM operating at an accelerating voltage of 20 keV, which was equipped with an EDAX silicon dri detector. XEDS spectrum quanti cation was conducted using EDAX Genesis so ware employing appropriate atomic number (Z), absorption (A) and uorescence (F) corrections.[26]

Synchrotron X-ray powder diffraction patterns obtained at beamline 11-BM of the Advanced Photon Source at Argonne National Labs, were utilized to determine the crystal structure and mean crystallite size of the as synthesized material. Rietveld re nement of this data was performed using the GSAS package[27] with EXPGUI interface[28] and the peak shapes were tted to the Lorentzian isotropic crystallite size, LX, strain broadening, LY, and Lorentzian anisotropic crystallite size broadening, ptec, parameters in GSAS Pro le 3. The mean crystallite size was then derived from the calculated LX parameter.

The phase stability of the crystallites at elevated temperature was determined using an Anton Paar DHS1100 domed hot stage attachment to a PANalytical Empyrean X-ray diffractometer. The sample holder was heated from 50–750 C collecting spectra at 100 C intervals with a 15 min dwell time at each temperature. Spectra were collected over a 30–100 2q angular range.

Raman spectra were collected at room temperature using a Witec alpha300 RA (Knoxville, TN, USA) confocal Raman microscope equipped with a 532 nm laser. The laser was focused to a 5 mm^2 spot on the dried $Cu_xCe_{1-x}O_{2-d}$ sample using a 20 objective lens. Spectra were collected using a UHTS 400NIR spectrometer with a diffraction grating having 2400 lines per mm.

Samples for analysis by scanning transmission electron microscopy (STEM) were prepared by drop casting some diluted aqueous sol onto a carbon coated molybdenum mesh TEM grid (Electron Microscopy Sciences). The samples were analyzed in an aberration corrected JEOL ARM 200CF analytical electron microscope equipped with a JEOL Centurio XEDS system operating at 200 kV. Images were collected in high angle annular dark eld (HAADF)-STEM and high-resolution HR-TEM modes. Fast Fourier Transforms (FFTs) derived from the HAADF-STEM and HR-TEM images were used to measure interplanar spacing and angles.

As-synthesized and dried $Cu_xCe_{1-x}O_{2-d}$ samples and those annealed at 300 C for 15 min in air were analyzed by X-ray photoelectron spectroscopy (XPS). The samples were attached to the sample holder with conductive carbon tape. XPS spectra were collected using a Scienta ESCA-300 system with an exci-tation energy of 1486.6 eV (Al Ka). The operating pressure of the sample chamber is in the range of 10^{-8} Torr which may lead to a slight reduction of the sample materials. High resolution scans were collected from the Ce (3d), Cu (2p), O (1s) and C (1s) spectral regions, along with a lower resolution wide survey scan of the entire spectrum. All spectra were calibrated to the C (1s) line of adventitious carbon (284.8 eV). The relative concentra-tions of Ce(III) and Ce(IV) were calculated semi-quantitatively by integrating the area under the peaks associated with Ce(III) (u^0, v^0, u^0, and v^0) and Ce(IV) (u, v, u'', v'', u''', and v''') following the method proposed by Zhang et al.,[29] in which, peak centers were set and only peak intensity and width were le as free parameters for peak tting. The peak width and integrated area values obtained were found to be in good agreement with those reported in prior literature.[29–32]

Catalytic testing

CeO_{2-d} or $Ce_{1-x}Cu_xO_{2-d}$ nanoparticles were loaded onto 105–150 mm silica support particles (Sigma Aldrich) through incip-ient wetness impregnation from a washed solution of nano-particles buffered in 20 mM citric acid at pH 5.5. The vacuum dried supported catalyst was packed into a 4 mm inner diameter quartz reactor tube and held in place with quartz wool plugs. Prior to any catalytic tests being performed, the reactor temperature was ramped at 10 C min^{-1} from 30 to 450 C in owing air to remove residual water and citrate capping ligands from the catalyst particles. TGA analysis showed removal of water and citrate capping ligands to occur at 100 C and 150–300 C respectively (Fig. S1†).

CO oxidation light-off curves were measured utilizing 500 mg of the supported catalyst (1% w/w) in a gas mixture of 2% CO, 8% O_2 and 90% Ar at a total ow rate of 37.5 mL min^{-1}. The reactor temperature was raised at 10 C min^{-1} from 30–450 C. Gas analysis was performed using a Cirrus 2 benchtop quad-rupole mass spectrometer (MKS instruments) at the reactor outlet monitoring for m/z ¼ 28, 32 and 44 signals which were assigned to CO, O_2 and CO_2 respectively.

Water gas shi reaction rate measurements were performed utilizing 500 mg of supported catalyst (7.5% w/w) in a gas mixture of 1.5% CO, 1.5% H_2O, and 97% N_2 at various ow rates chosen to be between 25 and 100 mL min^{-1}. The inlet gas composition and ow rate were controlled by mass ow controllers and H_2O was added to the stream by owing a portion of the N_2 gas through a sparger containing DI water at 25 C. The gas composition at the reactor outlet was analyzed by an in-line model 8610C gas chromatograph (SRI Instruments) equipped with thermal conductivity and ame ionization detector. Samples were heated to 450 C and the conversion measured stepwise at decreasing temperature intervals of 25 C. Calculations for activation energy used only data collected where conversion level was less than 15%. The measured rates were normalized to the BET surface area of the catalysts as determined by N_2 adsorption measurements at 196 C using a homemade instrument.

Results

Direct formation of the oxide is possible due to the intermediate bond strength of the lactic acid ligand with the cerium ion. Lactic acid bonds to cerium with a binding constant ($\log(K_1)$) of 2.756 allowing the pH to be adjusted to 8.5–9.0 before solid formation.[33] During particle synthesis, clear sols were formed a er pH adjustment as shown in Fig. 2a. Laser light scattering, which is indicative of colloidal sol formation, became visible within minutes accompanied by a change in color, which was dependent on the copper content. Sols with low nominal copper contents (i.e., x ¼ 0 to 0.01) transition from colorless to pale yellow whereas the samples with higher copper content (i.e., x ¼

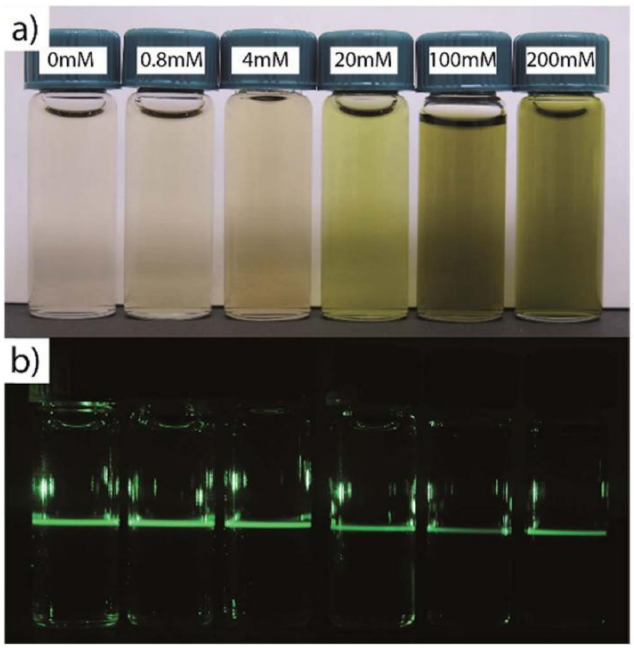

Fig. 2 Photograph of copper-doped ceria sols taken under (a) natural light and (b) green laser illumination. The copper nitrate content used during synthesis increases from 0 mM to 200 mM from left to right while the cerium nitrate concentration for each sample remained constant at 100 mM. The color of the washed sol changes from clear to pale yellow to green with increasing copper content. The laser scattering demonstrates the presence of colloidal nanocrystals.

0.05 to 0.35) transition from blue to deep green. Following synthesis, dialysis and washing, the nanoparticles were sus-pended in a dilute citric acid buffer solution (pH: 5.5, <20 mM) where they once again become clear with light scattering visible under laser illumination, Fig. 2b. A plot quantifying the relative proportions of precipitated-to-unprecipitated metal precursor for each sample composition prepared is shown in Fig. S2,† as determined by inductively coupled plasma mass spectrometry of the dialysis products.

In contrast to ceria precipitation, attempting to form pure cuprous oxide nanoparticles using a similar approach led to the generation of a clear Cu(II) complex when the ammonium hydroxide base was added (Fig. S3†). While the solution color intensity changed, there was no indication of precipitation or sol formation, suggesting a simple exchange of the complex ligand, from lactate to ammonia. Interestingly, this by-passes the formation of a solid cupric hydroxide precipitate that is expected to occur in the intermediate pH range in the absence of lactic acid[34] which supports the notion that the lactate ligand plays a stabilizing role in our synthesis procedure for $Ce_{1-x}Cu_xO_{2-d}$.

SEM-XEDS spectra were collected from dialyzed, washed and dried precipitated lms of the as-synthesized nanocrystals, Fig. 3a. All of the samples showed a strong series of Ce L-series peaks. The intensity of the Cu K_a and K_b peaks increased with increasing concentration of Cu nitrate in the synthesis solution. The corresponding copper concentrations in the set of Cu_x-$Ce_{1-x}O_{2-d}$ samples were determined on a metals basis using the

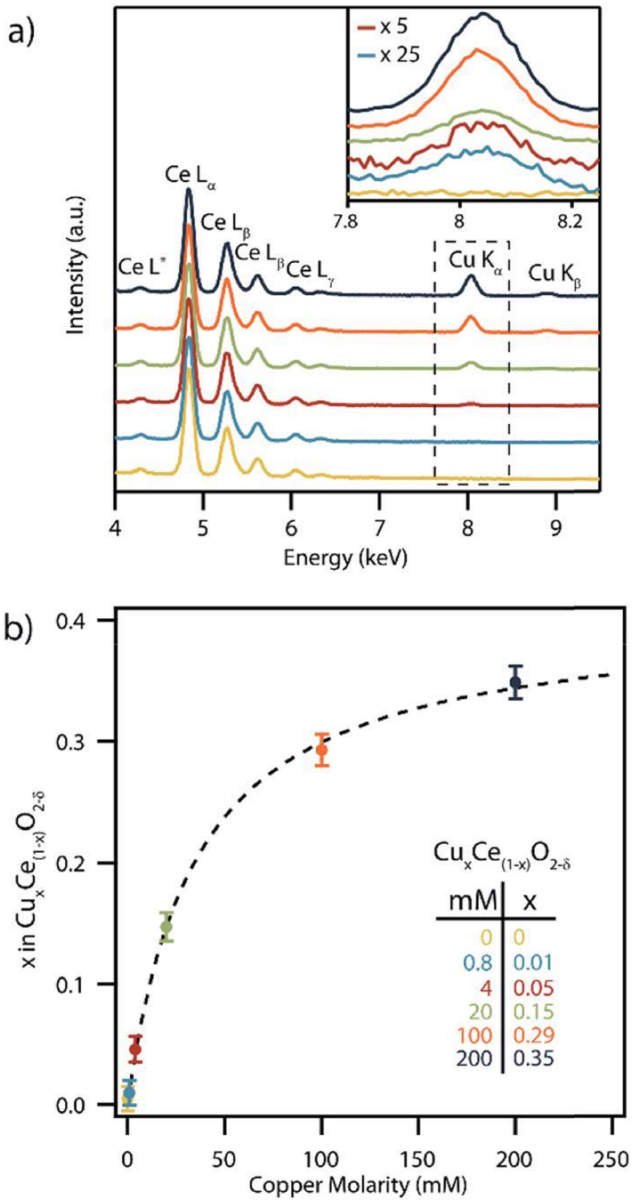

Fig. 3 (a) SEM-XEDS spectra collected from copper-doped ceria samples prepared with varying concentrations of copper nitrate in solution during synthesis. The inset in (a) shows a magnified view of the spectral range encompassing the Cu K_a peak (0.8 mM and 4 mM peaks multiplied by 25 and 5 times respectively). The color key for these spectra is inset in (b). (b) Measured copper content, x, in $Cu_xCe_{1-x}O_{2-d}$ nanoparticles, derived from analysis of the XEDS data presented in (a), as a function of Cu nitrate precursor concentration. The Ce nitrate precursor concentration was held constant at 100 mM in all samples.

standardless ZAF correction method,[35] Fig. 3b. The highest measured copper concentration corresponded to x ¼ 0.35 which is amongst the highest reported to date in $Cu_xCe_{1-x}O_{2-d}$.[36–38] While XEDS and ICP-MS (Fig. S2†) shows that most of the copper is incorporated into the $Cu_xCe_{1-x}O_{2-d}$ precipitate for low concentration samples (i.e., x ¼ 0.01, 0.05), the production of $Cu_xCe_{1-x}O_{2-d}$ particles with Cu higher concentrations required the copper precursor to be in excess, and thus much of the precursor remains unprecipitated. It should also be noted

that if we calculate the expected composition of the nano-crystals utilizing the ratios of precipitated materials determined from the ICP-MS data, we arrive at Cu contents greater than those experimentally determined by XEDS. This is due to the precipitation of a separate copper hydroxide phase that is removed from the particles a er synthesis by a triplicate washing procedure. The apparent saturation of Cu content at x ¼ 0.35 in the nanoparticles for higher Cu nitrate precursor concentrations is consistent with prior research that suggested a maximum Cu content of x ¼ 0.30 is sustainable within single phase $Ce_{1-x}Cu_xO_{2-\delta}$.[39]

Rietveld re nement of synchrotron X-ray diffraction (XRD) patterns obtained from the as-synthesized material with varying Cu contents con rmed the presence of a single phase with the uorite structure, space group Fm3m, in each sample (Fig. 4). There was no evidence of secondary CuO or Cu_2O phases in any of the samples, Fig. S4.† The average crystallite size was found to decrease with increasing Cu content, with the 1.7 nm mean size measured for the x ¼ 0.35 sample being amongst the smallest ever reported for either pure or doped ceria nano-crystals.[6,40,41] The ability to access such small crystallite sizes is a direct consequence of the absence of any calcination step in our synthesis procedure, which removes the opportunity for sintering and growth processes to occur. Decreasing crystallite size typically leads to an increase in the lattice parameter in pure CeO_2 particles.[42] In the present case, this is counter-balanced by the expected decrease in lattice parameter upon increasing the concentration of the lower radius Cu(II) ions replacing the larger Ce(III) and Ce(IV) ions $Cu_xCe_{1-x}O_{2-\delta}$.[43] The Shannon ionic radii of Cu(II), Ce(III) and Ce(IV) in an octahedral coordination environment are 0.73, 1.01 and 0.87 A respec-tively.[44] In our systematic set of materials, the in uence of copper concentration on lattice parameter is dominant which leads to a progressive decrease in lattice parameter except for the x ¼ 0–0.01 Cu concentration range where the in uence of size dominates and leads to a larger lattice parameter. Note that this result was con rmed by repeating the synthesis procedure and XRD measurements several times.

Fig. 5a and b show representative HAADF-STEM micro-graphs of the pure ceria material con rming the crystalline and nanoparticulate nature of the as-synthesized material. The measured interplanar spacing and angles derived from the corresponding fast Fourier transform (FFT, inset in Fig. 5a) match well with those expected for the [110] projection on the CeO_2 uorite structure, Fig. S5.† The ceria particles have a relatively narrow size distribution with an average particle size of 4.2 0.7 nm measured as a surface-equivalent spherical diameter (Fig. 5c) which matches well with the value derived from the XRD data (Fig. 4).

Fig. 5d–f show the corresponding HAADF-STEM micro-graphs and particle size distribution of the nanocrystals in the $Cu_{0.05}Ce_{0.95}O_{2-\delta}$ sample. As with the pure ceria material, the interplanar spacing and angles derived from the FFT inset in Fig. 5d match well with the uorite structure; this time viewed along the [112] projection, Fig. S6.† The particle size distribu-tion is narrow (Fig. 5f), with a mean particle size of 3.7 0.7 nm,

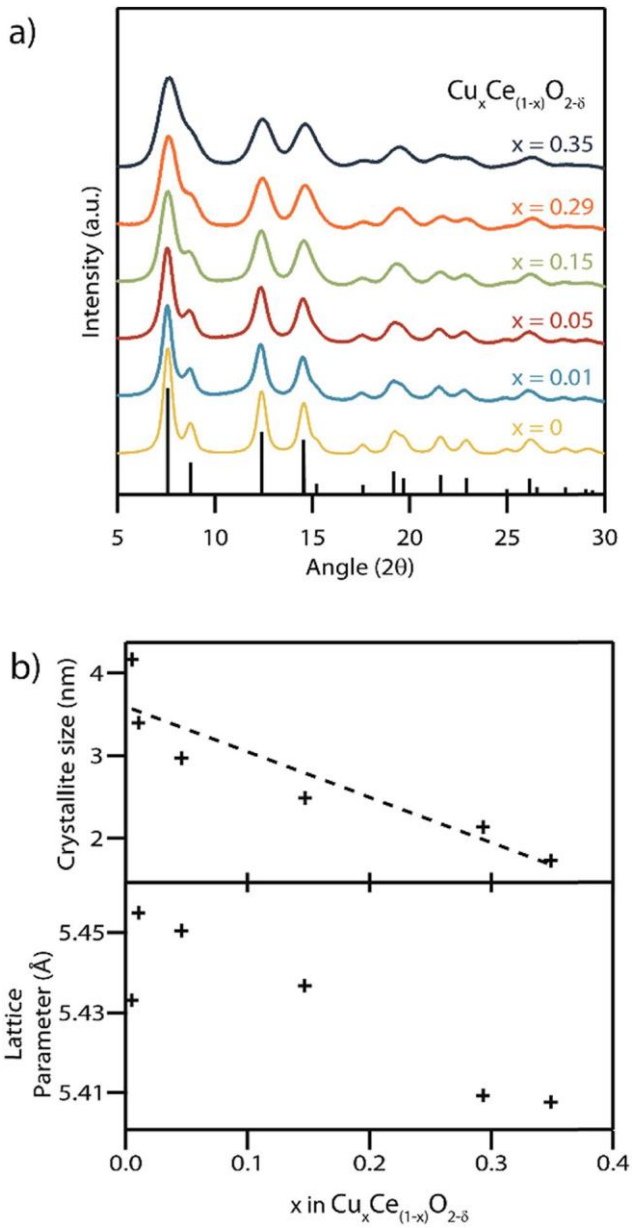

Fig. 4 (a) Synchrotron X-ray diffraction patterns of the as-synthesized $Cu_xCe_{1-x}O_{2-\delta}$ materials with varying Cu content showing good agreement with the CeO_2 fluorite structure, space group 3 , (ICSD collection code 156250, reference peak positions shown). The progressive broadening of the peaks with increasing copper content is indicative of decreasing crystallite mean size. The trend line is provided as a guide to the eye. (b) Lattice parameter and crystallite size measurements derived from Rietveld refinement of the XRD patterns presented in (a).

which again matches well with the corresponding value derived from XRD analysis (Fig. 4).

Raman spectra acquired from the pure $CeO_{2-\delta}$ material exhibit a single peak centered at 470 nm ^{1}, Fig. 6a, which is consistent with the reported position of the single allowed Raman mode of ceria with the uorite structure.[45,46] This F_{2g} symmetry peak has previously been assigned to an oxygen anion breathing mode around the central cation.[46] This peak was

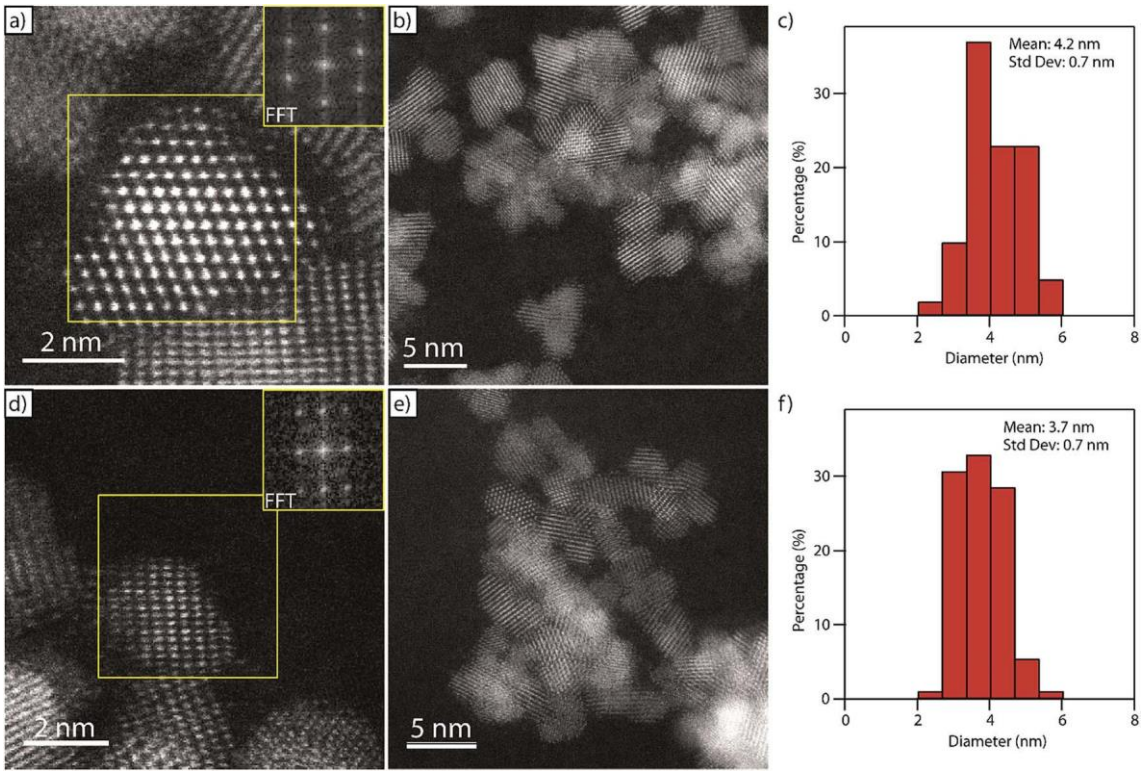

Fig. 5 Representative HAADF-STEM images of (a, b) CeO_{2-d} and (d, e) $Cu_{0.05}Ce_{0.95}O_{2-d}$ nanoparticles showing high crystallinity. The inset FFTs in (a) and (d), obtained from the areas in the yellow boxes, are consistent with the [110] and the [112] projections of fluorite structured ceria respectively. Surface-equivalent spherical diameter particle size distributions of the pure ceria and copper-doped ceria nanoparticles are shown in (c) and (f) respectively.

observed to both broaden and systematically shi to lower wavenumber in an approximately linear fashion as the Cu content in the series of $Cu_xCe_{1-x}O_{2-d}$ samples increases, Fig. 6b. The F_{2g} peak position decreased to 455 cm^{-1} for the x ¼ 0.35 Cu-doped sample. This is trend is fully consistent with the formation of a solid solution of copper within ceria.[1,46] Peak broadening with increasing Cu content can be attributed to increased disorder due to the random distribution of both copper cations and oxygen vacancies in the material and their effect on neighboring Ce–O bond strength.[4] A portion of this increased peak width can also be attributed to the observed decrease in crystallite size that typically increases the peak width in nanomaterials.[47] Additionally, from wide-range Raman spectra (Fig. S7†) no Cu_2O (150, 230, and 640 cm^{-1}) or CuO (290, 340, and 625 cm^{-1}) peaks were detected, further con rming that a single phase solid solution material forms upon doping CeO_2 with Cu. Also visible in the wide range Raman spectra is a wide band peak at 600 cm^{-1}, which can be attributed to oxygen vacancies in the samples.[1]

In order to further con rm the formation of a solid solution and the potential impact on catalytic activity, the in uence of Cu doping on the Ce oxidation state and oxygen vacancy concentration in the as-synthesized materials was investigated by XPS. While this is typically described as a surface charac-terization technique, we can in this case consider the spectra to be representative of the bulk due to the mean nanoparticle diameter being smaller than the XPS penetration depth. A representative spectrum of the Ce (3d) region for the $Cu_{0.29}Ce_{0.71}O_{2-d}$ sample is shown in Fig. 7a with the spectra for all of the other materials in the series presented in Fig. S8.† Cerium was found to exist in both the Ce(III) and Ce(IV) oxidation states which is typical of nanoscale ceria.[42] The concentration of Ce(III) was determined semi-quantitatively by taking a ratio of the area under the curve of tted Ce(III) peaks over that of the summed areas of the Ce(III) and Ce(IV) peaks, following a method previ-ously described by Zhang et al.[29] This analysis indicates a trend of decreasing Ce(III) concentration with increasing copper content, varying from 56% in pure CeO_{2-d} to 48% in the highest doped $Cu_{0.35}Ce_{0.65}O_{2-d}$ sample, Table 1. The Ce(III) concentra-tion values obtained were found to be in good agreement with those reported in prior literature.[42,48]

Fig. 7b shows the XPS spectra of the Cu (2p) region for the complete set of $Cu_xCe_{1-x}O_{2-d}$ samples. The x ¼ 0.05, 0.15, 0.29, and 0.35 samples showed clear Cu $2p_{1/2}$ and Cu $2p_{3/2}$ peaks with only weak satellite peaks at 945 eV, indicative of primarily a Cu(I) oxidation state with only small quantities of Cu(II).[49] The minor amount of Cu(II) may be indicative of a small amount of a segregated Cu-containing secondary phase in these highest Cu-content materials.[50] As expected, no Cu (2p) peaks were observed in the x ¼ 0 nanocrystals. Similarly, no Cu (2p) peaks were observed in the x ¼ 0.01 sample due to the detection limit constraints of the XPS instrument.

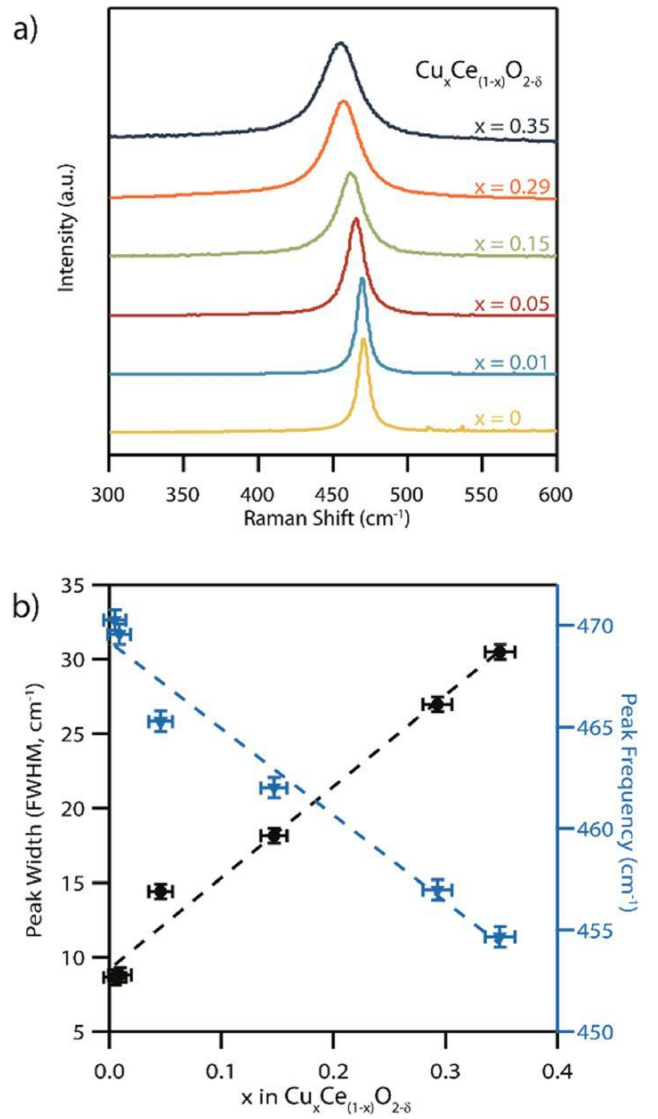

Fig. 6 (a) Raman spectra of the as-synthesized CeO_2 and copper-doped ceria samples showing peak broadening and a progressive shift to lower frequencies in the Ce–O band peak position as the copper content increases, which is consistent with the formation of a solid solution. (b) Corresponding Ce–O Raman peak full-width-at-half-maximum (FWHM) and peak frequency as a function of copper content extracted from the data in (a).

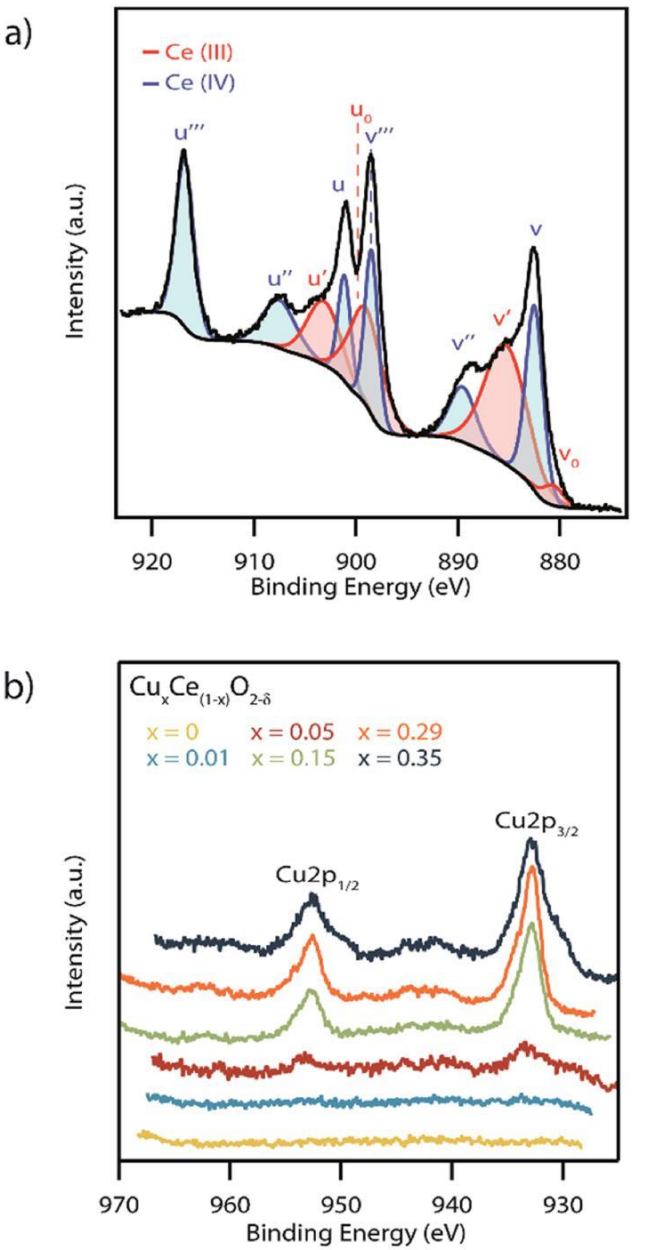

Fig. 7 (a) X-ray photoelectron spectra of the 29 mol% copper doped ceria sample in the Ce (3d) region. Peaks attributed to both Ce(III) (red) and Ce(IV) (blue) can be seen which can only be accommodated if there are also oxygen vacancies present in the crystal lattice. (b) XPS spectra of the Cu (2p) region of the entire set of $Cu_xCe_{1-x}O_{2-\delta}$ samples with x varying from 0 to 0.35. The absence of strong Cu(II) satellites at 942 and 962 eV indicates that copper exists in the Cu(I) oxidation state.

A key bene t of the lactic acid mediated synthesis approach employed in this study is the direct formation of the mixed Cu_x-$Ce_{1-x}O_{2-\delta}$ nanocrystals at room temperature, removing the need for a high temperature calcination step that can lead to unwanted crystallite growth and possible exsolution of Cu from the solid solution. However, many catalytic applications of these materials will typically require that they be exposed to elevated tempera-tures. High temperature XRD patterns obtained upon heating the $Cu_xCe_{1-x}O_{2-\delta}$ samples in air were analyzed to determine the extent of crystal growth and the stability of the mixed oxide phase as a function of calcination temperature. The Scherrer equation was used to estimate the average crystallite size from the (220) and (311) re ections of CeO_2 using a shape factor of 0.9.[51,52]

Fig. 8a and b shows XRD of the systematic set of spectra for the $Cu_{0.15}Ce_{0.85}O_{2-\delta}$ and $Cu_{0.35}Ce_{0.65}O_{2-\delta}$ materials at a series of calcination temperatures beginning at 50 C and increasing up to 750 C at 100 C intervals with a 15 min dwell time at temperature before taking any measurements. A distinct nar-rowing of the peaks characteristic of the uorite structure was noted for each sample with increasing temperature due to crystallite growth at these elevated temperatures (Fig. 8c). The secondary set of XRD peaks at 750 C and 450 C respectively for

Table 1 Physical characteristics of the various $Cu_xCe_{1-x}O_{2-d}$ materials

Nominal copper concentration[a] (mM)	Actual copper concentration[b] (metals basis)	Mean crystallite size[c] (nm)	Lattice parameter[c] (A)	Ce(III) concentration[d] (%)	Raman peak (cm^{-1})
0	—	4.2	5.433	56%	470.3
0.8	0.01	3.4	5.455	56%	469.6
4	0.05	3.0	5.450	54%	465.3
20	0.15	2.5	5.437	50%	462.0
100	0.29	2.1	5.409	46%	457.0
200	0.35	1.7	5.408	48%	454.7

[a] Concentration of $Cu(NO_3)_2$ used during synthesis. [b] Determined from XEDS measurements. [c] Calculated from Rietveld re nement of synchrotron powder XRD data. Standard deviations in the lattice parameter, obtained from GSAS, are an order of magnitude lower than the lowest reported digit. [d] Determined using XPS data from the Ce (3d) energy range, following the method proposed by Zhang et al.[29]

$Cu_{0.15}Ce_{0.85}O_{2-d}$ and $Cu_{0.35}Ce_{0.65}O_{2-d}$ can be indexed to CuO, indicating an upper thermal limit of phase stability for these solid solutions. No CuO phase formation was observed for any of the other lower Cu content nanocrystals up to the maximum measurement temperature of 750 C. The source of this CuO phase can be attributed either to the exsolution of Cu from these higher Cu-content $Cu_xCe_{1-x}O_{2-d}$ nanocrystals, or the subsequent crystallization of an amorphous Cu phase formed during synthesis. Such an amorphous Cu phase cannot be detected by XRD or by STEM, although we note the possible indication of the existence of some amorphous material in the as-XPS data acquired from the as-synthesized $Cu_{0.29}Ce_{0.81}O_{2-d}$ sample (Fig. 7).

Fig. 9 shows the XPS spectra of the Cu (2p) region for the series of copper-doped ceria samples that have been calcined at 300 C for 15 min. Samples with low copper concentrations show no signi cant Cu (2p) peaks. The heat-treated variants of the more highly doped samples show characteristic Cu $2p_{1/2}$ and Cu $2p_{3/2}$ peaks along with the Cu(II) satellites indicating the copper in the sample has changed oxidation state from Cu(I) to Cu(II). Likewise, there is an average shi in binding energy of +0.6 eV in the Cu $2p_{3/2}$ peaks a er heat treatment, further indicating this switch in oxidation state.[49] Such a change in oxidation state has been re-ported previously by Scir´e et al. in copper-doped ceria materials that were heated from 200 to 400 C.[53] Taken together with our data this indicates that the transition from Cu(I) to Cu(II) occurs somewhere between 200–300 C.

The CO oxidation reaction is typically used as an important benchmark for the catalytic activity of these Cu-doped ceria materials.[54] The CO oxidation light-off curves shown in Fig. 10a exhibit the anticipated trend of lower light-off temperature, indicative of higher catalytic activity, with increasing copper content in the $Cu_xCe_{1-x}O_{2-d}$ structure. The exception to this trend occurs for the highest copper content material, i.e., $Cu_{0.35}Ce_{0.65}O_{2-d}$, which shows a slight decrease in the copper light-off temperature relative to the $Cu_{0.29}Ce_{0.71}O_{2-d}$ sample, most likely due to the formation of some CuO secondary phase as indicated by our high temperature XRD experiments. The $Cu_{0.29}Ce_{0.71}O_{2-d}$ catalyst showed 50% conversion at 145 C with a gas hour space velocity of 25 000 h^{-1}. Hence the performance of our $Cu_{0.29}Ce_{0.71}O_{2-d}$ material is in-line with other literature reports on copper-doped ceria CO oxidation catalysts.[6,55]

CO oxidation light-off experiments were repeated for the $Cu_{0.29}Ce_{0.71}O_{2-d}$ sample following calcination at a series of elevated temperatures. The $Cu_{0.29}Ce_{0.71}O_{2-d}$ sample was chosen for this experiment because it was the highest performing catalyst of the series and because it had been shown, through high temperature XRD, to develop CuO crystals a er calcination at elevated temperatures. The CO oxidation performance of this particular catalyst was unaffected at calcination temperatures below 550 C; however, a signi cant decrease in the activity was observed a er calcination at 650 C which was attributable to copper exsolution (Fig. 10b).

An Arrhenius plot of the reaction rate for the water gas shi reaction using the set of $Cu_xCe_{1-x}O_{2-d}$ samples is shown in Fig. 10c. These reaction rates have been normalized using the surface areas determined from BET isotherm analysis (Table 2). As with the CO oxidation light-off data, the catalytic activity generally increases with increasing Cu content in the Cu_x-$Ce_{1-x}O_{2-d}$ material, as shown in Fig. S9.† The measured decrease in activation energy was accompanied by an increase in overall reaction rate as x increased in $Cu_xCe_{1-x}O_{2-d}$ up to x ¼ 0.29. Again, as with the CO light-off data, the overall rate of the x
¼ 0.35 decreases when compared with the x ¼ 0.29 sample, however the activation energy slightly decreases. This further indicates a decrease in accessibility of more active solid solution sites caused by exsolution of copper. Representative STEM micrographs of the $Cu_{0.35}Ce_{0.65}O_{2-d}/SiO_2$ materials before and a er the WGS oxidation reaction are shown in Fig. S10.† The images clearly show some evidence of crystallite growth in the post-reaction sample. Although, the presence of any thin amorphous layers of exsoluted copper rich material could not be detected in either sample, >10 nm segregated copper phase was detected in the post reaction sample. The measured acti-vation energies and reaction rates for the WGS reaction are also competitive with previous literature reports for copper-doped ceria catalysts.[56]

Discussion

The nature of the precipitate formed upon raising the pH of a metal nitrate solution is qualitatively described in a classic paper by Livage et al.[24] As the pH increases, the interaction of the metal with the aqueous solution transitions from “aquo”

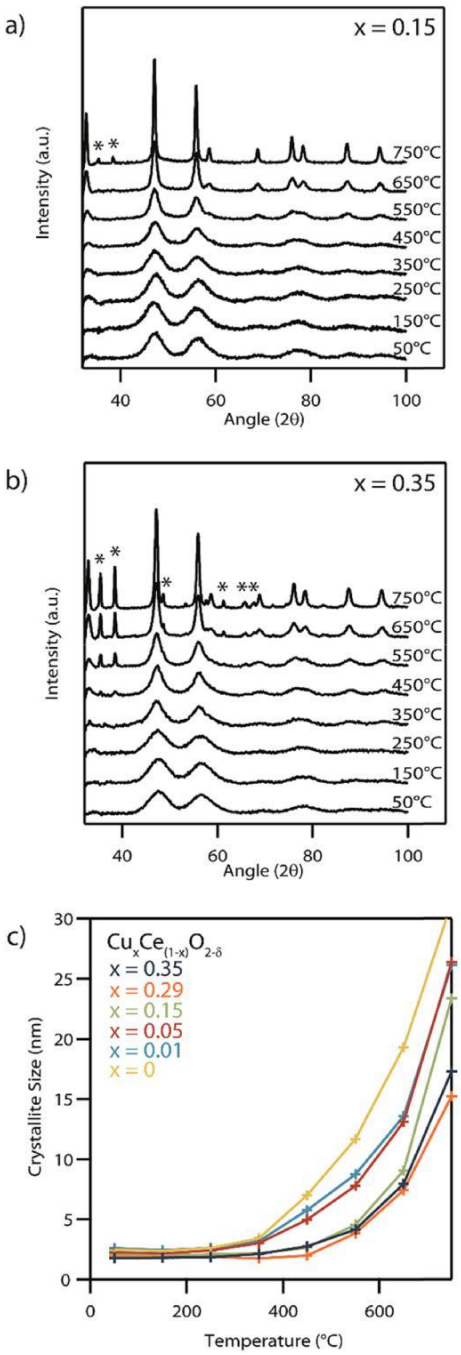

Fig. 8 Series of X-ray diffraction spectra of (a) x ¼ 0.15 and (b) x ¼ 0.35 copper-doped $Cu_xCe_{1-x}O_{2-d}$ samples after being subjected to calci-nation at increasing temperatures in air for a 15 min dwell time. As the calcination temperature increases, the diffraction peaks get narrower due to crystal growth effects. In the samples with the highest copper-doping levels distinct copper oxide (labelled *) peaks begin to appear after calcination at elevated temperatures. (c) Plot showing the mean ceria crystallite size as a function of calcination temperature. High copper concentrations seem to hinder sintering of the fluorite-type $Cu_xCe_{1-x}O_{2-d}$ phase.

(M–OH_2) to "hydroxo" (M–OH) and nally to "oxo" (M–O), with the precise pH required for a 'transition' being a function of the identity of the transition metal itself and the associated ligands

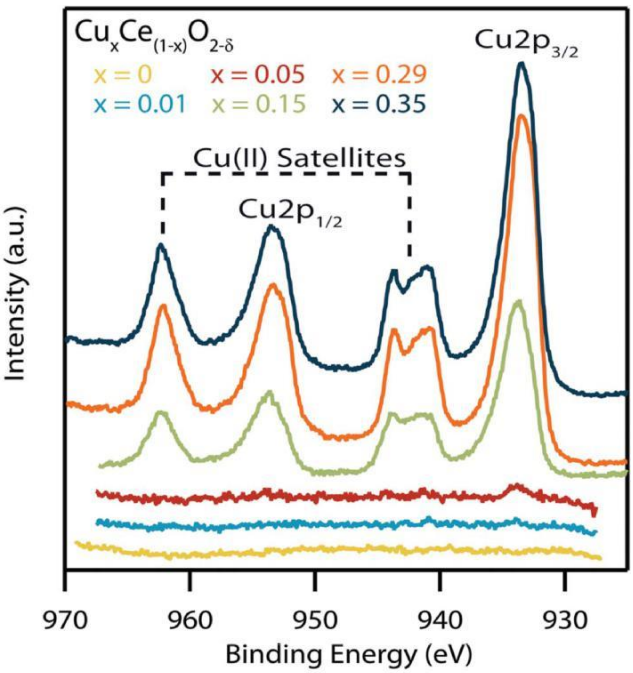

Fig. 9 XPS spectra of the Cu (2p) region of the various copper-doped ceria samples after calcination at 300 C for 15 min. The presence of strong satellite peaks indicate a shift in Cu from the Cu(I) to the Cu(II) oxidation state after heat treatment.

in solution. In a typical ceria nanoparticle synthesis procedure, the pH of the precursor solution is raised to the point where it induces precipitation of insoluble cerium hydroxide nano-crystals by shi ing into the 'hydroxo' region of Livage's construction. The hydroxide precipitate can then subsequently be transformed into cerium oxide by a suitable calcination treatment.

Our results demonstrate that the addition of lactic acid into the precursor solution strongly in uences the ligand associated with the cerium ion in solution. The binding constants (log(K_1)) of nitrate and lactate ligands to Ce(III) are 0.21 and 2.756 (ref. 33) respectively, indicating a substantially stronger association of the lactic acid species to the Ce(III) cation.[38] We suggest that the direct formation of the oxide in our lactic acid mediated synthesis route is due to the stronger ligand association that stabilizes the cation in solution as the pH increases upon the addition of ammonium hydroxide. This shi s the point of precipitation out of the 'hydroxo' region into the 'oxo' region in the Livage diagram.

The exact nature of the catalytically active site in $Cu_xCe_{1-x}O_{2-d}$ is still a matter of debate, however, there is general consensus that formation of a mixed Ce–Cu–O solid solution is critical to creating highly active sites. While it can be challenging to prove the formation of a true solid solution at very low dopant concentrations, all of the experimental evidence collected points to the formation of an intimately mixed $Cu_xCe_{1-x}O_{2-d}$ phase for x ¼ 0.01 to 0.35 in our as-synthesized materials. The lattice parameter determined from the synchrotron XRD data (Fig. 4) shows a progressive decrease in lattice parameter of the uorite-type with increasing Cu

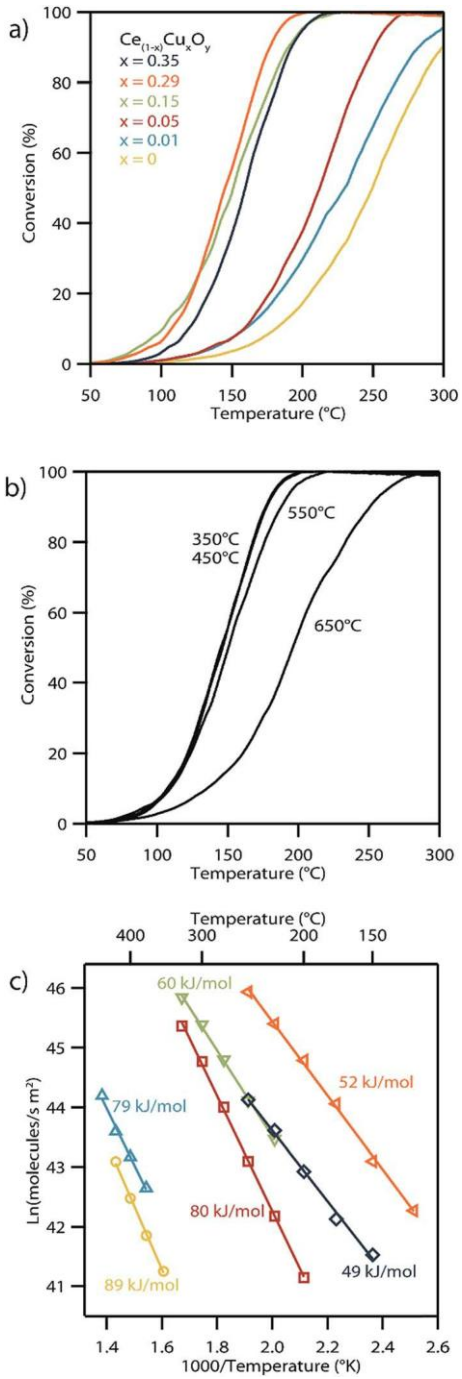

Fig. 10 (a) CO conversion data as a function of temperature for the set of $Cu_xCe_{1-x}O_{2-d}$ materials (with x varying from 0 to 0.35) sup-ported on silica. The temperature required for 50% conversion ranges from 262 C for CeO_{2-d} to 145 C for $Cu_{0.29}Ce_{0.71}O_{2-d}$. (b) The CO conversion curves for $Cu_{0.29}Ce_{0.71}O_{2-d}$ materials that had been subjected to calcination at varying temperatures. It should be noted that a significant reduction in catalytic activity is only apparent for samples calcined above 650 C (note: the 350 C and 450 C curves strongly overlap). (c) Arrhenius plot analyses of water gas shift rates for the set of $Cu_xCe_{1-x}O_{2-d}$ materials (with x varying from 0 to 0.35) supported on silica for a CO : H_2O : N_2 gas mixture of 1.5 : 1.5 : 97% at 1 atm.

content as would be expected from a Vegard's law type rela-tionship due to the smaller cationic radius of Cu. Furthermore, no secondary phases were observed in the as-synthesized materials prepared via our lactic acid mediated synthesis.

Further evidence for Cu–Ce–O solid solution formation comes from the approximately linear decrease in Ce–O breathing mode Raman frequency with increasing dopant level x in the $Cu_xCe_{1-x}O_{2-d}$ phase (Fig. 6). This is the result of the shi in phonon frequencies due to the decrease in lattice parameter, o en referred to as the Grunier¨ shi in Raman frequency.[46] The concurrent broadening of the Raman peaks with increasing doping level is also indicative of solid solution formation, where such broadening is due to substitutional disorder on the cation sublattice upon Cu-doping leading to a distribution of cation–anion breathing frequencies.[46] While the trends in lattice parameter, crystallite size and Raman spectra strongly indicate the formation of mixed oxide solid solution nanocrystals, we cannot fully rule out that some surface segregated amorphous copper-rich material exists in the as-synthesized $Cu_xCe_{1-x}O_{2-d}$ materials with x ¼ 0.29 and 0.35.

We also note that the Ce(III) to Ce(IV) ratio in our materials shows a systematic trend of increasing Ce(IV) content with increasing Cu(I) doping level in $Cu_xCe_{1-x}O_{2-d}$, suggesting some charge compensation occurs to stabilize the oxygen within the lattice upon doping. Finally, we found no evidence of secondary Cu–O phases in any of our HAADF-STEM imaging experiments on the as-synthesized materials (Fig. 5). When combined with the measured catalytic efficacy of the materials, all of the experimental evidence strongly supports the conclusion that the lactic acid mediated synthesis route forms solid solution $Cu_xCe_{1-x}O_{2-d}$ nanoparticles.

The nominal Cu content chosen during synthesis also has a strong in uence on the resulting nanocrystal size, evidenced, for example, by the 29% decrease in crystallite size upon doping with only 5% Cu into the ceria nanocrystals. The only signi cant differences during the synthesis of these two materials relative to that of pure CeO_2 is (i) the addition of 4 mM copper nitrate and (ii) a 5% increase in lactic acid concentration to maintain the lactic acid : cation ratio. Analysis of mean particle size as a function of lactic acid concentration used (Fig. S11†) demonstrates that the in uence of this process parameter is negligible. The mean crystallite size however shows a near linear relationship with the amount of copper in solid solution (Fig. 4) and there are two possible reasons for this eff ect. As shown in Fig. S3,† rather than leading to precipitation of a cuprous oxide, addition of ammonium hydroxide to a precursor solution containing only copper nitrate stimulates the formation of a complex between the Cu(II) and ammonium ion. Such a strong ligand–cation interaction may retard particle growth when Cu is included as the ammonium covers the surface of the growing particle. Alternatively, this Cu-complex may serve to nucleate particle formation, leading to rapid formation of a large number of small nuclei. Further work with alternative cationic dopant species, such as Ni, Fe, or Co, is required to fully understand the eff ect of dopant identity upon

Table 2 Catalytic performance characteristics of the various Cu_x-$Ce_{1-x}O_{2-d}$ materials supported on SiO_2

Sample[a]	Surface area[b] (m^2 g^{-1})	CO light-off temperature[c] (°C)	WGS activation energy[d] (kJ mol^{-1})
CeO_{2-d}	155	262	89.0 1.2
$Cu_{0.01}Ce_{0.99}O_{2-d}$	190	250	78.8 2.4
$Cu_{0.05}Ce_{0.95}O_{2-d}$	145	212	80.0 1.1
$Cu_{0.15}Ce_{0.85}O_{2-d}$	110	151	59.9 0.6
$Cu_{0.29}Ce_{0.71}O_{2-d}$	90	145	51.6 0.5
$Cu_{0.35}Ce_{0.65}O_{2-d}$	90	159	49.2 0.9

[a] Copper concentration calculated from XEDS measurements. [b] Calculated from N_2 adsorption isotherms. [c] Temperature for 50% CO conversion. [d] Calculated by Arrhenius equation from data collected at under 15% conversion.

nanocrystal nucleation and growth using our lactic acid medi-ated synthesis method.

The $Cu_{0.35}Ce_{0.65}O_{2-d}$ material is comprised of particles with a mean size of 1.7 nm as determined by XRD, which is amongst the smallest ever reported for Cu doped-ceria material.[6,40,41] The ability to form such small crystallites is most likely due to the direct formation of the oxide during the low temperature precipitation stage, removing the need for a calcination step at an elevated temperature, thus avoiding unnecessary sintering. The materials display high surface areas due to their ultra-small crystallite sizes, up to 190 m^2 g^{-1} for the $Cu_{0.01}Ce_{0.99}O_{2-d}$ sample, Table 2. There is an increase in surface area in the x ¼ 0 to 0.01 copper concentration range due to a decrease in crystallite size from 4.2 to 3.4 nm respectively. The subsequent decrease in surface area at higher values of x may be attributed to an increased propensity for sintering of the higher Cu-content nanocrystals upon sample pre-treatment as evidenced by the narrowing of the XRD peak widths in Fig. 8.

While our experimental evidence points to the as-synthesized products being Cu–Ce–O solid solutions, these materials, particularly with the higher Cu dopant levels, become unstable at high temperature. XRD indicates phase separation upon calcination at 750 °C for lightly doped $Cu_{0.15}Ce_{0.85}O_{2-d}$ formulation, whereas the second phase appeared more readily at 450 °C for the higher doped $Cu_{0.35}Ce_{0.65}O_{2-d}$ material (Fig. 8). This indicates why high Cu dopant levels may be diffi-cult to achieve using more traditional synthesis routes where an elevated temperature calcination step is required.

The XRD calcination series study also suggests slower ceria crystallite growth in samples containing higher copper concentrations, although this may be partly due to exsolution of the Cu to form secondary CuO_x, leading to a loss of material from the parent $Cu_xCe_{1-x}O_{2-d}$, nanoparticles.

The in uence of copper doping level on the catalytic activity of $Cu_xCe_{1-x}O_{2-d}$, is clearly observable for the both water–gas-shi and CO oxidation reactions (Fig. 10). For the water gas shi reaction, the overall reaction rate increases with increasing Cu loading up to x ¼ 0.29 the $Cu_{0.29}Ce_{0.71}O_{2-d}$ sample, but then decreases for the $Cu_{0.35}Ce_{0.65}O_{2-d}$ composition. However, it should be noted that these materials were calcined at 450 °C prior to these catalytic tests, which is the temperature at which phase segregation of CuO_x occurs from $Cu_{0.35}Ce_{0.65}O_{2-d}$, implying that the decrease in reaction rate is associated with this bulk phase segregation. This concept is reinforced by analyzing CO oxidation light-off curves for the $Cu_{0.29}Ce_{0.71}O_{2-d}$ material with interme-diate sintering steps of increasing temperature, Fig. 10b. The CO light-off temperature is stable until a calcination temperature of 650 °C is reached, at which point the subsequent light-off temperature then increases. This again corresponds to the temperature at which the formation of a distinct CuO_x second phase is observed in the XRD pattern for $Cu_{0.29}Ce_{0.71}O_{2-d}$. This effect has been noted in a previous CO oxidation study using ceria doped with high concentrations of copper.[57] It has also been shown that under certain conditions, copper has a tendency to segregate to the surface of nanoparticles when doped into ceria.[2] Higher concentrations of copper on the particle surface will most likely lessen the accessibility to ceria, which is essential to provide oxygen for the reaction.

Conclusions

The facile lactic acid mediated approach for synthesizing Cu-doped ceria nanoparticles described here demonstrates the potential of using base precipitation as a synthesis route for con-trollably preparing nanoscale mixed oxide materials. By utilizing an intermediate binding strength ligand, intimately mixed $Cu_{1-x}Ce_xO_{2-d}$ solid solution crystals can be formed directly at room temperature in aqueous solution with high dopant concen-trations and crystallite sizes as low as 1.7 nm. The synthesis method outlined uses low cost, easily accessible precursors and can be easily be implemented in any chemistry lab or scaled-up for industrial production. Our synthesized particles also show competitive catalytic activity for the water gas shi and CO oxida-tion reactions when compared to more conventionally prepared counterpart materials that have been described in the literature.

Conflicts of interest

There are no con icts to declare.

Acknowledgements

This material presented is the result of research work supported by the National Science Foundation under the EFRI-PSBR program, Grant No. 1332349 and the Lehigh University Accel-erator program. Use of the Advanced Photon Source at Argonne National Laboratory was supported by the U. S. Department of Energy, Office of Science, Office of Basic Energy Sciences, under Contract No. DE-AC02-06CH11357. We are grateful to Dr Ste-phen C. Peters for his assistance with ICP-MS measurements.

References

1 W. Wang, P. Du, S. Zou, H. He, R. Wang, Z. Jin, S. Shi, Y. Huang, R. Si and Q. Song, ACS Catal., 2015, 5, 2088–2099.

2 J. S. Elias, N. Artrith, M. Bugnet, L. Giordano, G. A. Botton, A. M. Kolpak and Y. Shao-Horn, ACS Catal., 2016, 6, 1675– 1679.

3 D. Gamarra, C. Belver, M. Fern´andez-Garc´ıa and A. Mart´ınez-Arias, J. Am. Chem. Soc., 2007, 129, 12064–12065.
4 D. Gamarra, G. Munuera, A. B. Hungr´ıa, M. Fern´andez-Garc´ıa, J. C. Conesa, P. A. Midgley, X. Q. Wang, J. C. Hanson, J. A. Rodr´ıguez and A. Mart´ınez-Arias, J. Phys. Chem. C, 2007, 111, 11026–11038.
5 W. Liu and M. Flytzani-Stephanopoulos, Chem. Eng. J., 1996, 64, 283–294.
6 Y. Li, Q. Fu and M. Flytzani-Stephanopoulos, Appl. Catal., B, 2000, 27, 179–191.
7 X. Wang, J. A. Rodriguez, J. C. Hanson, D. Gamarra, A. Martnez-Arias and M. Fernndez-Garca, J. Phys. Chem. B, 2005, 109, 19595–19603.
8 D. S. Newsome, Catal. Rev.: Sci. Eng., 1980, 21, 275–318.
9 N. Schumacher, A. Boisen, S. Dahl, A. A. Gokhale, S. Kandoi, L. C. Grabow, J. A. Dumesic, M. Mavrikakis and I. Chorkendorff, J. Catal., 2005, 229, 265–275.
10 V. Polshettiwar and R. S. Varma, Green Chem., 2010, 12, 743–754.
11 G. Centi, P. Ciambelli, S. Perathoner and P. Russo, Catal. Today, 2002, 75, 3–15.
12 M. Cargnello, V. V. Doan-Nguyen, T. R. Gordon, R. E. Diaz, E. A. Stach, R. J. Gorte, P. Fornasiero and C. B. Murray, Science, 2013, 341, 771–773.
13 X. Wang, J. A. Rodriguez, J. C. Hanson, D. Gamarra, A. Mart´ınez-Arias and M. Fern´andez-Garc´ıa, J. Phys. Chem. B, 2006, 110, 428–434.
14 J. Guzman, S. Carrettin and A. Corma, J. Am. Chem. Soc., 2005, 127, 3286–3287.
15 S. Scir´e, S. Minico, C. Crisafulli, C. Satriano and A. Pistone, Appl. Catal., B, 2003, 40, 43–49.
16 S. Golunski, R. Rajaram, N. Hodge, G. J. Hutchings and C. J. Kiely, Catal. Today, 2002, 72, 107–113.
17 A. Trovarelli, Catal. Rev.: Sci. Eng., 1996, 38, 439–520.
18 W. Liu and M. Flytzani-Stephanopoulos, J. Catal., 1995, 153, 317–332.
19 W. J. Stark, L. M¨adler, M. Maciejewski, S. E. Pratsinis and A. Baiker, Chem. Commun., 2003, 5, 588–589.
20 V. S. Escribano, E. F. L´opez, M. Panizza, C. Resini, J. M. G. Amores and G. Busca, Solid State Sci., 2003, 5, 1369–1376.
21 J. Lee and S. Choi, Mater. Lett., 2004, 58, 390–393.
22 A. Migani, G. N. Vayssilov, S. T. Bromley, F. Illas and K. M. Neyman, Chem. Commun., 2010, 46, 5936–5938.
23 S. Carrettin, P. Concepcin, A. Corma, J. M. Lpez Nieto and V. F. Puntes, Angew. Chem., Int. Ed., 2004, 43, 2538–2540.
24 J. Livage, M. Henry and C. Sanchez, Prog. Solid State Chem., 1988, 18, 259–341.
25 T. D. Golden and A. Q. Wang, J. Electrochem. Soc., 2003, 150, C624.
26 H. Yakowitz, in Practical Scanning Electron Microscopy, ed. nonymous, Springer, U.S.A., 1975, pp. 327–372.
27 A. C. Larson and R. B. Von Dreele, General Structure Analysis System (GSAS), Los Alamos National Laboratory Report LAUR 86-748, 2000.
28 B. H. Toby, J. Appl. Crystallogr., 2001, 34, 210–213.
29 F. Zhang, P. Wang, J. Koberstein, S. Khalid and S. Chan, Surf. Sci., 2004, 563, 74–82.
30 A. Laachir, V. Perrichon, A. Badri, J. Lamotte, E. Catherine, J. C. Lavalley, J. El Fallah, L. Hilaire, F. Le Normand and E. Qumr, J. Chem. Soc., Faraday Trans., 1991, 87, 1601–1609.
31 M. Romeo, K. Bak, J. El Fallah, F. Le Normand and L. Hilaire, Surf. Interface Anal., 1993, 20, 508–512.
32 F. Larachi, J. Pierre, A. Adnot and A. Bernis, Appl. Surf. Sci., 2002, 195, 236–250.
33 A. E. Martell and L. G. Sillen, Stability Constants Supplement No. 1, The Chemical Society, London, 1971.
34 L. Hidmi and M. Edwards, Environ. Sci. Technol., 1999, 33, 2607–2610.
35 S. Reed, Br. J. Appl. Phys., 1965, 16, 913.
36 W. Shan, W. Shen and C. Li, Chem. Mater., 2003, 15, 4761–4767.
37 S. Ho˘cevar, U. O. Kra˘sovec, B. Orel, A. S. Arico and H. Kim, Appl. Catal., B, 2000, 28, 113–125.
38 M. Jobbgy, F. Marino, B. Schnbrod, G. Baronetti and M. Laborde, Chem. Mater., 2006, 18, 1945–1950.
39 K. Pemartin-Biernath, A. V. Vela-Gonzlez, M. B. Moreno-Trejo, C. Leyva-Porras, I. E. Castaeda-Reyna, I. Jurez-Ramrez, C. Solans and M. Snchez-Domnguez, Materials, 2016, 9, 480.
40 D. Andreeva, I. Ivanov, L. Ilieva, M. V. Abrashev, R. Zanella, J. W. Sobczak, W. Lisowski, M. Kantcheva, G. Avdeev and K. Petrov, Appl. Catal., A, 2009, 357, 159–169.
41 L. Yue and X. Zhang, J. Alloys Compd., 2009, 475, 702–705.
42 S. Deshpande, S. Patil, S. V. Kuchibhatla and S. Seal, Appl. Phys. Lett., 2005, 87, 133113.
43 A. Aranda, E. Ayln, B. Solsona, R. Murillo, A. M. Mastral, D. R. Sellick, S. Agouram, T. Garca and S. H. Taylor, Chem. Commun., 2012, 48, 4704–4706.
44 R. D. Shannon, Acta Crystallogr., Sect. A: Cryst. Phys., Diffr., Theor. Gen. Crystallogr., 1976, 32, 751–767.
45 L. D. Jadhav, M. G. Chourashiya, A. P. Jamale, A. U. Chavan and S. P. Patil, J. Alloys Compd., 2010, 506, 739–744.
46 J. R. McBride, K. C. Hass, B. D. Poindexter and W. H. Weber, J. Appl. Phys., 1994, 76, 2435–2441.
47 G. Gouadec and P. Colomban, Prog. Cryst. Growth Charact. Mater., 2007, 53, 1–56.
48 S. Tsunekawa, K. Ishikawa, Z. Li, Y. Kawazoe and A. Kasuya, Phys. Rev. Lett., 2000, 85, 3440.
49 S. Poulston, P. M. Parlett, P. Stone and M. Bowker, Surf. Interface Anal., 1996, 24, 811–820.
50 M. Monte, G. Munuera, D. Costa, J. C. Conesa and A. Martnez-Arias, Phys. Chem. Chem. Phys., 2015, 17, 29995–30004.
51 U. Holzwarth and N. Gibson, Nat. Nanotechnol., 2011, 6, 534.
52 P. Scherrer, Nachr. Ges. Wiss. Goettingen, Math.-Phys. Kl., 1912, 2, 98–100.
53 S. Scir´e, C. Crisafulli, P. M. Riccobene, G. Patan and A. Pistone, Appl. Catal., A, 2012, 417, 66–75.
54 H. Freund, G. Meijer, M. Scheffler, R. Schl¨ogl and M. Wolf, Angew. Chem., Int. Ed., 2011, 50, 10064–10094.
55 S. Royer and D. Duprez, ChemCatChem, 2011, 3, 24–65.
56 E. T. Saw, U. Oemar, X. R. Tan, Y. Du, A. Borgna, K. Hidajat and S. Kawi, J. Catal., 2014, 314, 32–46.
57 F. Wang, R. Buchel,€ A. Savitsky, M. Zalibera, D. Widmann, S. E. Pratsinis, W. Lubitz and F. Schuth,€ ACS Catal., 2016, 6, 3520–3530.